Topological surface states above the Fermi level in Hf$_2$Te$_2$P

T. J. Boyle,[1] A. Rossi,[1,2] M. Walker,[1] P. Carlson,[1] M. K. Miller,[1] J. Zhao,[1] P. Klavins,[1] C. Jozwiak,[2] A. Bostwick,[2]
E. Rotenberg,[2] V. Taufour,[1] I. M. Vishik,[1] and E. H. da Silva Neto[1,*]

[1]*Department of Physics, University of California, Davis, California 95616, USA*
[2]*Advanced Light Source, Lawrence Berkeley National Laboratory, Berkeley, California 94720, USA*

We report a detailed experimental study of the band structure of the recently discovered topological material Hf$_2$Te$_2$P. Using the combination of scanning tunneling spectroscopy and angle-resolved photoemission spectroscopy with surface K doping, we probe the band structure of Hf$_2$Te$_2$P with energy and momentum resolution above the Fermi level. Our experiments show the presence of multiple surface states with a linear Dirac-like dispersion, consistent with the predictions from previously reported band-structure calculations. In particular, scanning tunneling spectroscopy measurements provide experimental evidence for the strong topological surface state predicted at 460 meV, which stems from the band inversion between Hf-d and Te-p orbitals. This band inversion comprised of more localized d states could result in a better surface-to-bulk conductance ratio relative to more traditional topological insulators.

Topological quantum phases have been discovered in a variety of materials such as topological insulators, Dirac and Weyl semimetals, and nodal line semimetals [1–5]. All of these topological phases result in nontrivial topological surface states (SSs), which could be used for future low-dissipation electronic or spintronic technologies [2,6,7]. Although several materials that host one of the aforementioned topological phases have been discovered, quantum materials that exhibit several SSs at distinct regions of energy-momentum space are not common. Recently, band-structure calculations and experiments indicate a rich phenomenology of topological electronic states in Zr$_2$Te$_2$P [8] and in Hf$_2$Te$_2$P [9], including multiple SSs. In particular, for Hf$_2$Te$_2$P, the calculations find four SSs as follows, where the energies are relative to the Fermi level (E_F): three dispersions at the Γ point near 0.46 eV (SS1), 0.17 eV (SS2), −1.2 eV (SS3), and a Dirac-node arc along the Γ-M direction, centered at the M point near −0.9 eV (SS4). Similar features (SS1, SS2, and SS4) were also predicted in Zr$_2$Te$_2$P. This unusual multitude of states in a single material stems from the topological character of various bulk bands originating from Te-p and Hf-d orbitals. Following Fu and Kane [10], the four topological $\mathbb{Z}_2$ invariants were computed from the calculated band structure. From this analysis, SS4 at −0.9 eV was identified to have a weak topological $\mathbb{Z}_2$ invariant, while SS1 at 0.46 eV yields a strong $\mathbb{Z}_2$ invariant. The topological nature of SS2 and SS3 could not be clearly resolved, with SS2 displaying a significant bulk-surface mixing [9].

Among the SSs in Hf$_2$Te$_2$P, SS1 at 0.46 eV may be the one with the greatest potential toward future applications for several reasons. First, excluding SS2 due to its surface-bulk mixing, SS1 is the closest state to the Fermi level of Hf$_2$Te$_2$P. Second, it is the only SS centered within a clear direct gap

in the bulk. Third, its topological nature originates from the inversion of Te-p and Hf-d orbitals, which could lead to a better surface-to-bulk conduction ratio when compared to more traditional topological insulators like Bi$_2$Te$_3$ or Bi$_2$Se$_3$, where only p orbitals are involved [8,9,11]. This favorable surface conduction stems from the more localized nature of the Hf-d (or Zr-d in the case of Zr$_2$Te$_2$P) states, leading to a higher effective mass for the bulk electrons when compared to Bi$_2$Te$_3$ or Bi$_2$Se$_3$, or even to the other SSs in Hf$_2$Te$_2$P that do not involve Hf-d orbitals. Additionally, this would render the interesting combination of topology and strong electron correlations, if E_F is tuned to within the pseudogap.

Experimentally, the SSs in Zr$_2$Te$_2$P and Hf$_2$Te$_2$P below the Fermi level, E_F, have been resolved through angle-resolved photoemission spectroscopy (ARPES) measurements, showing a remarkable agreement to the band-structure predictions [8,9]. However, since ARPES experiments are not able to probe the SS1 state above the Fermi level, this key topological state still lacks direct experimental evidence.

Here, we use two methods to experimentally access the states above E_F and provide direct evidence for SS1 in Hf$_2$Te$_2$P. First, through the deposition of K atoms we electron-dope the surface of the material, enabling ARPES to measure states up to approximately 160 meV above the original E_F. Second, we use scanning tunneling microscopy and spectroscopy (STM/S) to measure energy-resolved quasiparticle interference (QPI) patterns on the surface of Hf$_2$Te$_2$P, which allows us to probe the energy-momentum structure both above and below E_F [12–19]. Using our combined ARPES and STM/S data, and their comparison to the reported surface band-structure calculations, we resolve the SSs of Hf$_2$Te$_2$P above E_F and identify Dirac-like dispersive bands centered at 170 and 460 meV, where the SS1 and SS2 states have been predicted.

Single crystals of Hf$_2$Te$_2$P were grown from vapor transport following the synthesis developed for the isostructural

*ehda@ucdavis.edu
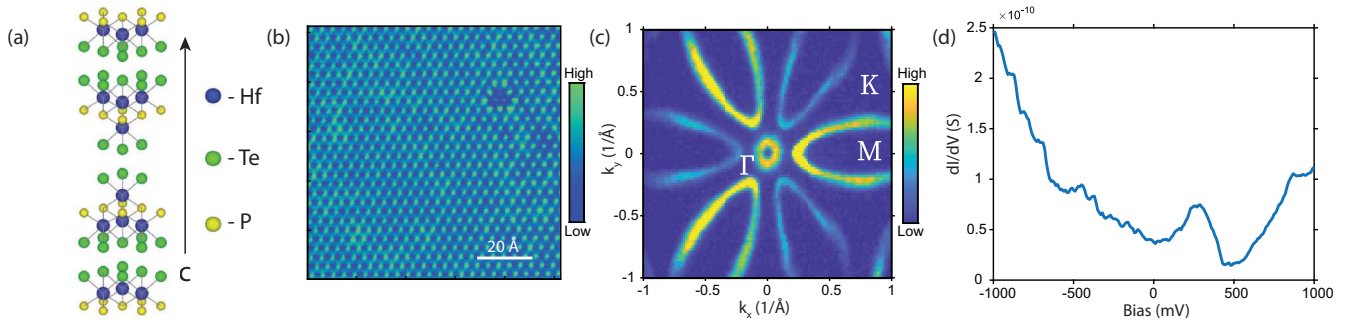
FIG. 1. (a) Crystal structure of Hf_2Te_2P. (b) STM topography taken at -120 mV sample bias and 700 pA current set point. (c) Fermi surface of a pristine sample measured by ARPES. (d) STS measured dI/dV spectrum with current and bias set points of 450 pA and -1.5 V.

Zr_2Te_2P [20,21], also detailed in Ref. [22]. ARPES experiments were performed in ultrahigh vacuum (UHV) at beamline 7.0.2 MAESTRO at the Advanced Light Source. The μ-ARPES endstation allows for a spot size of 80 μm $\times$ 80 μm, which is crucial to scanning a homogeneous region in a cleaved area. After growth, the Hf_2Te_2P crystals were sealed in an inert environment, transferred into a glovebox at the beamline and cleaved. From the glovebox, they were transferred into the ARPES chamber without air exposure and cleaved a second time *in situ*. The measurements were done at 77 K with a photon energy of 100 eV. The sample surface was doped with K using a commercial SAES alkali-metal dispenser. STM/S measurements were done with a customized Unisoku USM-1300 instrument. The samples were cleaved *in situ* in a UHV environment with pressures below 1×10^{-9} Torr. All STM/S measurements were performed at 4.2 K.

Figure 1(a) shows the crystal structure of Hf_2Te_2P, where the atoms between consecutive Te layers along the c axis are bonded by weak van der Waals forces. This makes the Te layer the most likely termination resulting from the cleaving process [9]. Figure 1(b) shows an atomically resolved STM constant-current topography on a cleaved surface of Hf_2Te_2P, featuring a hexagonal structure with lattice constants that are consistent with those obtained from x-ray diffraction [22]. Localized defects are observed, appearing as depressions in the topography, as well as smoother features which may reflect underlying defects. We note that scanning multiple crystals, and many distinct microscopic regions within each cleave, we have only observed the Te termination in the STM measurements. Using the same *in situ* cleaving process, our ARPES measurements yield the occupied electronic structure of Hf_2Te_2P. Figure 1(c) displays the result of the ARPES measured Fermi surface, which shows a holelike pocket centered at the Γ point and electronlike flower patterns, consistent with previous measurements. Overall, the momentum distribution curves show extremely sharp features which, together with the atomic resolution obtained in STM measurements, indicate the high quality of the surfaces obtained from the cleaving process [21]. Figure 1(d) shows a representative measurement of the differential conductance, dI/dV, which is proportional to the density of states as a function of energy. The most prominent feature in the spectrum is a pseudogap centered around 500 mV, with a small but nonzero density of states that could have surface and/or bulk origin.

First we focus on SS2, which is predicted near 170 meV at the Γ point [9]. To access states above E_F with ARPES, we deposited K atoms on the cleaved surface of Hf_2Te_2P, which occupy the states above E_F and enables their photoemission [23]. Figures 2(a)–2(e) show the evolution of the constant energy contours for positive energies where zero refers to the Fermi level of the sample before K doping [21]. The data in Figs. 2(a)–2(e) indicate the collapse of the hole pocket into a single point at Γ, which is more clearly observed in the dispersion plot through $k_y = 0$, Fig. 2(g), and could not be resolved without the K doping; compare to data in Fig. 2(f), prior to K doping.

We also confirm the presence of the surface state at 170 meV via STS measurements of QPI patterns. Figures 3(a)–3(c) show dI/dV maps for different energies above E_F over a large field of view, 120 nm $\times$ 120 nm. The maps were taken by measuring dI/dV while performing bias sweeps from 700 to -100 meV with 20-meV steps on a 256×256 spatial grid. It is evident from the STS maps that the characteristic length scales of the modulations in the local density of states (LDOS) are much larger than the interatomic distance and are strongly energy dependent. This last behavior is typical of quasiparticle interference where the modulations are characterized by an energy-dependent wave vector $\vec{Q}(E) = \vec{k}_f(E) - \vec{k}_i(E)$, where $\vec{k}_{i,f}(E)$ are determined by the band structure. The two-dimensional Q-space structure of the LDOS is obtained by Fourier transformation of the STS maps, $\tilde{g}(Q, E)$, as seen in Figs. 3(d)–3(f) [21]. Note that $\tilde{g}(Q, E = 80$ meV) roughly features a hexagonal shape, while $\tilde{g}(Q, E = 160$ meV) more closely matches a star shape, Figs. 3(d)–3(f), which more clearly conveys the energy dependence of the real-space QPI patterns. We note that other techniques that can also probe the unoccupied electronic states, such as inverse photoemission, two-photon photoemission spectroscopy, and time-resolved ARPES, suffer from limitations in energy resolution, difficulties in the interpretation of nonequilibrium states and related dynamics, and may be restricted to work only for a narrow range of materials. On the other hand, the QPI and K-doped ARPES measurements used for our studies probe the sample in its equilibrium state and can be done with high-energy resolution and to a wider range of materials.

We are able to quantitatively compare the results of the ARPES and STS measurements for energies between E_F and 160 meV, which is the range accessed by both K-doped
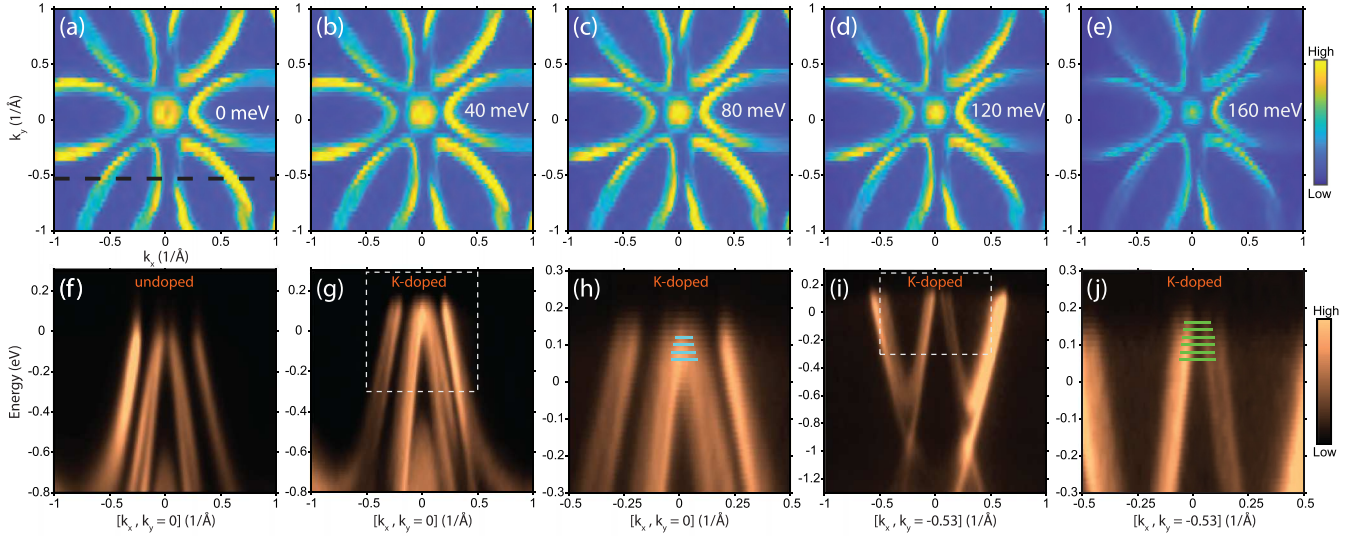
FIG. 2. (a)–(e) ARPES measured constant-energy contours of the K-doped sample for different positive energy values. (f) Band structure of the undoped sample along Γ-M. (g) Band structure of the doped sample along Γ-M. (h) Region highlighted by the gray box in (g) showing the Q vectors (cyan lines) associated with the hole pocket centered at Γ for four different energies. (i) Band structure along the direction of the dotted line in (a). (j) Region highlighted by the gray box in (i) showing the Q vectors (green lines) for five different energies. The appearance of duplicate bands in the K-doped data, when compared to the undoped sample, (f) and Fig. 1(c), can be attributed to multiple facets of the cleaved surface [21].

ARPES and STS. Line cuts of $\tilde{g}(Q, E)$ along the two high-symmetry directions show distinct peak features on top of a large background. For example, a line cut along $[Q_x = 0,$ $Q_y]$ at 240 meV reveals a distinct peak at 0.09 (1/Å), Figs. 4(a) and 4(b). From $\tilde{g}(Q, E)$, we construct QPI dispersion maps along the two high-symmetry directions, Fig. 4(c),
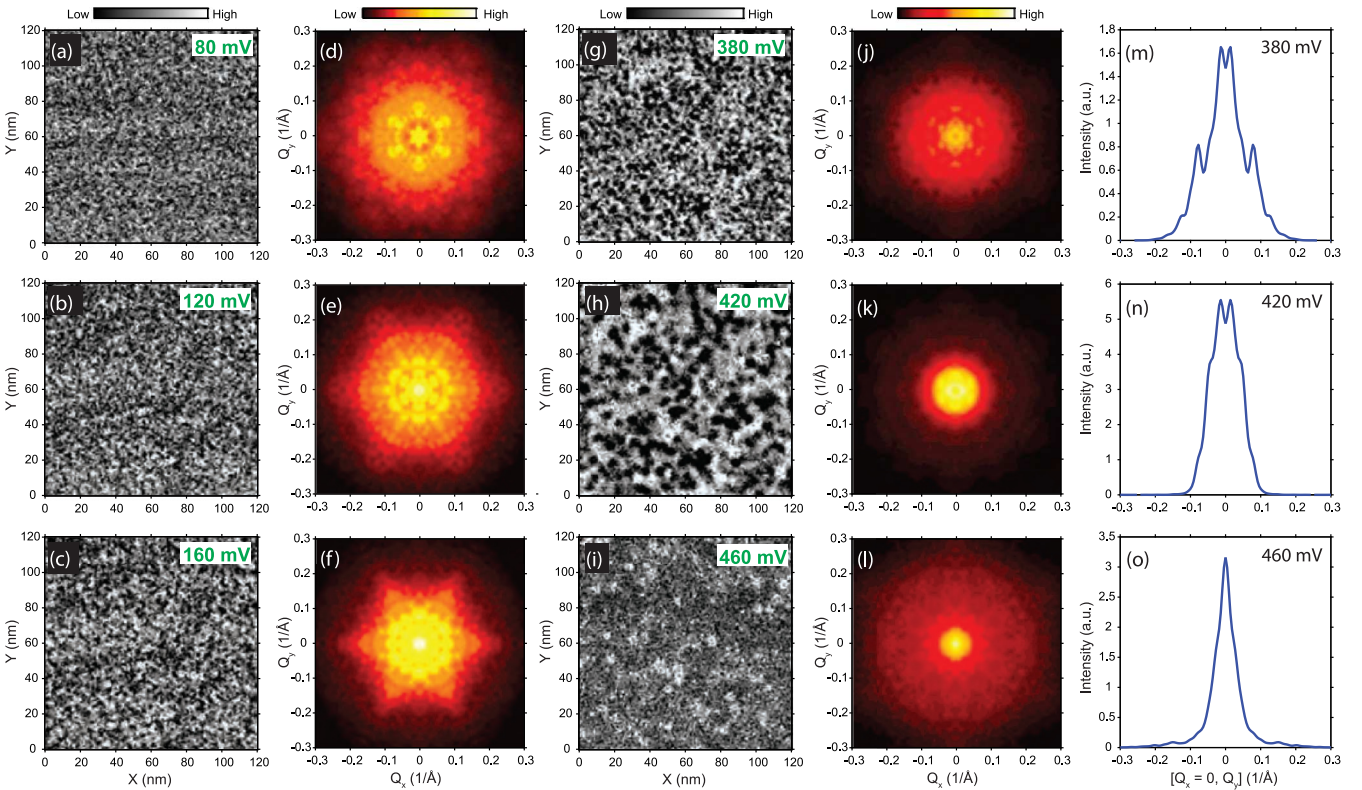

FIG. 3. (a)–(c) STS maps showing the real-space LDOS near 170 meV. (d)–(f) Fourier transforms of (a)–(c). (g)–(i) STS maps near 420 meV. (j)–(l) Fourier transforms of (g)–(i). (m)–(o) Line cuts along $[Q_x = 0, Q_y]$. The bias and current values were set to 800 mV and 500 pA, respectively, and the dI/dV signal was measured via a lock-in technique with a modulation amplitude of 10 mV.
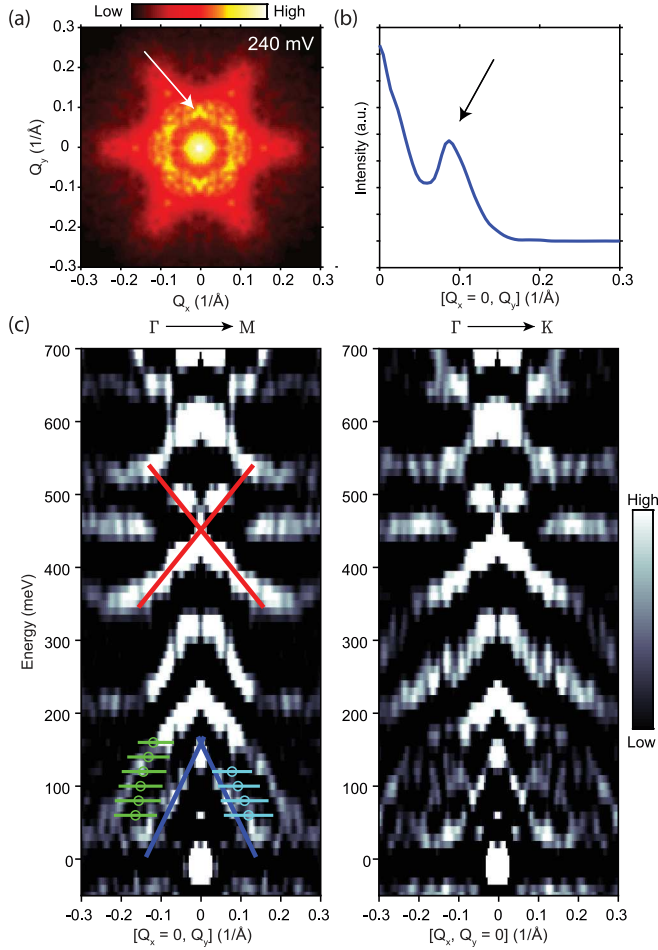
FIG. 4. (a) Fourier transform of the STS map at 240 mV. (b) Line cut of (a) along $[Q_x = 0, Q_y]$, showing a distinct peak at $Q_y = 0.09$ (1/Å). (c) QPI dispersion maps along the Γ-M and Γ-K directions. The ARPES measured Q vectors are overlaid by cyan and green dots (with solid line error bars) for the dispersion curves displayed in Figs. 2(h) and 2(j), respectively. Q-vector dispersions from the band-structure calculations along Γ-M are represented by the red and blue lines [9].

using the second-derivative method to clearly visualize the dispersive features. In the 0–220 meV range we observe two peaks which disperse inwards as a function of energy. A detailed comparison to the ARPES data indicates that the inner dispersive peak matches the intrapocket distance across Γ, while the outer peak dispersion more closely matches the separation between adjacent electron-pocket *petals* [see the cyan and green circles in Fig. 4(c), which correspond to the cyan and green lines in Figs. 2(h) and 2(j)]. In fact, ARPES cuts along $[k_x, k_y = -0.53]$ (1/Å) indicate a linear dispersion which extrapolates to a node near 220 meV [Figs. 2(i) and 2(j)]. A similar state has been observed in Zr_2Te_2P, with spin-orbit coupling expected to open a gap since the crossing is located away from time-reversal invariant momenta and is not protected by any crystalline symmetry [8]. Our STS measurements do not resolve the presence of a gap at 220 meV, although our resolution was limited to 10 meV. [The dI/dV was measured via a lock-in technique using a 10 mV modulation to the bias voltage.] Contrary to the

outer peak, the inner QPI feature originates from the band centered at Γ, a time-reversal invariant point, as further confirmed by the excellent agreement with reported band-structure calculations [blue line in Fig. 4(c)] [9]. Thus, our triple quantitative agreement between STS, ARPES, and theory confirm the presence of a Dirac-like dispersion centered at 170 meV.

Finally, we focus on SS1, the strong topological SS predicted near 460 meV. Although ARPES cannot access this state, even with K deposition, it can be resolved with STS measurements. First we note that although QPI signals can be the result of multiple surface or bulk bands, the calculated band structure of Hf_2Te_2P indicates that the highest energy SS near Γ exists inside a large bulk pseudogap (≈ 0.13 eV), consistent with the observed minimum in the tunneling DOS [Fig. 1(e)]. Focusing on that energy region, we observe a dramatic increase of the characteristic QPI wavelength as the bias is varied from 380 to 420 meV in our STS measurements [see Figs. 3(g) and 3(h)]. The same trend is observed in the Fourier transforms, Figs. 3(j) and 3(k), where a circular pattern shrinks toward $Q = 0$, reflecting the expected QPI pattern from an isolated Dirac cone. Then, the expectation is that precisely at the crossing $\tilde{g}(Q)$ should display a single peak at $Q = 0$, which becomes broad in the presence of disorder. Indeed, the real-space STS data in Fig. 3(i) shows a spatially inhomogeneous LDOS, due to the structural defects of the crystal, and a single central peak in the Fourier transform data, Fig. 3(l). This trend is summarized in Figs. 3(m)–3(o), which display line cuts of the data in Figs. 3(j)–3(l), showing $Q_y \neq 0$ peaks converging to a single point at 460 meV. We note that in the absence of a predominant $Q \neq 0$ QPI signal at 460 meV, $\tilde{g}(Q)$ displays a weak halo, Figs. 3(l) and 3(o), that stems from the intrinsic inhomogeneity of Hf_2Te_2P. Indeed, we find identical spatial patterns in both the $\tilde{g}(Q, E = 460$ meV) and the topographic map over the same area [21], which confirms the non-QPI origin of the halo in Fig. 3(l). Thus the intensity observed in the second-derivative map in Fig. 4(c) at $E = 460$ meV and $Q \approx \pm 0.17$ (1/Å) is not indicative of an additional band. Now focusing on the energy-dependent QPI signal at lower Q and comparing its energy dispersion to the prediction from calculations [red lines in Fig. 4(c)], we find a remarkable agreement, thus demonstrating the presence of the surface state with a node at 460 meV above E_F.

Our combined ARPES-STS measurements and their remarkable agreement with previous band-structure calculations indicate the presence of topological surface states above the Fermi level in Hf_2Te_2P. Although the topological nature of the various SSs and their spin texture still requires more direct evidence from, for example, spin-polarized ARPES [24] or STS near extended defects [25], the remarkable agreement to the reported band-structure calculations strongly suggests their topological nature. If these states are to be harnessed toward novel technologies, they need to be tuned to E_F by either chemical doping or surface gating. Here, the states above E_F uncovered by our studies may provide a more direct path to these technologies than the previously measured states at -0.9 eV. Also, the surface state centered at 460 meV is observed in the absence of other bands in our QPI measurement, suggesting a small contribution from the bulk,

although only detailed measurements of the electronic bulk properties would confirm this. Still, a high surface-to-bulk conductance ratio could be achieved in Hf_2Te_2P, since the strong topological nature of the surface state at 460 meV originates from the band inversion of Hf-d and Te-p orbitals, in contrast to traditional topological insulators. Note that the mixing Hf-d and Te-p orbital character, and its topology, may be tuned by chemical substitution, with the substitution of Hf (e.g., by Zr or Ti) controlling the d orbitals and the substitution of Te (e.g., by Se) regulating the p character, not to mention the modification of lattice parameters by doping the P site (e.g., by As) or by chemical intercalations between layers. Finally, since the current topological insulators suffer from contaminant conducting bulk channels that bypass the topologically protected surface states, the topological states uncovered by our studies may offer an alternative avenue for future applications.

[1] X.-L. Qi and S.-C. Zhang, Rev. Mod. Phys. **83**, 1057 (2011).

[2] M. Z. Hasan and C. L. Kane, Rev. Mod. Phys. **82**, 3045 (2010).

[3] Y. Ando, J. Phys. Soc. Jpn. **82**, 102001 (2013).

[4] N. P. Armitage, E. J. Mele, and A. Vishwanath, Rev. Mod. Phys. **90**, 015001 (2018).

[5] S.-Y. Yang, H. Yang, E. Derunova, S. S. P. Parkin, B. Yan, and M. N. Ali, Adv. Phys.: X **3**, 1414631 (2018).

[6] J. Alicea, Rep. Prog. Phys. **75**, 076501 (2012).

[7] L. Šmejkal, Y. Mokrousov, B. Yan, and A. H. MacDonald, Nat. Phys. **14**, 242 (2018).

[8] H. Ji, I. Pletikosić, Q. D. Gibson, G. Sahasrabudhe, T. Valla, and R. J. Cava, Phys. Rev. B **93**, 045315 (2016).

[9] M. M. Hosen, K. Dimitri, A. Kumar Nandy, A. Aperis, R. Sankar, G. Dhakal, P. Maldonado, F. Kabir, C. Sims, F. Chou, D. Kaczorowski, T. Durakiewicz, P. Oppeneer, and M. Neupane, Nat. Commun. **9**, 3002 (2018).

[10] L. Fu and C. L. Kane, Phys. Rev. B **76**, 045302 (2007).

[11] M. Yang and W.-M. Liu, Sci. Rep. **4**, 5131 (2014).

[12] J. E. Hoffman, K. McElroy, D.-H. Lee, K. M. Lang, H. Eisaki, S. Uchida, and J. C. Davis, Science **297**, 1148 (2002).

[13] Q.-H. Wang and D.-H. Lee, Phys. Rev. B **67**, 020511(R) (2003).

[14] P. Roushan, J. Seo, C. V. Parker, Y. S. Hor, D. Hsieh, D. Qian, A. Richardella, M. Z. Hasan, R. J. Cava, and A. Yazdani, Nature (London) **460**, 1106 (2009).

[15] I. Zeljkovic, Y. Okada, C.-Y. Huang, R. Sankar, D. Walkup, W. Zhou, M. Serbyn, F. Chou, W.-F. Tsai, H. Lin, A. Bansil, L. Fu, M. Hasan, and V. Madhavan, Nat. Phys. **10**, 572 (2014).

[16] A. Yazdani, E. H. da Silva Neto, and P. Aynajian, Annu. Rev. Condens. Matter Phys. **7**, 11 (2016).

[17] H. Inoue, A. Gyenis, Z. Wang, J. Li, S. W. Oh, S. Jiang, N. Ni, B. A. Bernevig, and A. Yazdani, Science **351**, 1184 (2016).

[18] H. Zheng, S.-Y. Xu, G. Bian, C. Guo, G. Chang, D. S. Sanchez, I. Belopolski, C.-C. Lee, S.-M. Huang, X. Zhang, R. Sankar, N. Alidoust, T.-R. Chang, F. Wu, T. Neupert, F. Chou, H.-T. Jeng, N. Yao, A. Bansil, S. Jia, H. Lin, and M. Z. Hasan, ACS Nano **10**, 1378 (2016).

[19] Z. Zhu, T.-R. Chang, C.-Y. Huang, H. Pan, X.-A. Nie, X.-Z. Wang, Z.-T. Jin, S.-Y. Xu, S.-M. Huang, D.-D. Guan, S. Wang, Y.-Y. Li, C. Liu, D. Qian, W. Ku, F. Song, H. Lin, H. Zheng, and J.-F. Jia, Nat. Commun. **9**, 4153 (2018).

[20] K. Tschulik, M. Ruck, M. Binnewies, E. Milke, S. Hoffmann, W. Schnelle, B. P. T. Fokwa, M. Gilleßen, and P. Schmidt, Eur. J. Inorg. Chem. **2009**, 3102 (2009).

[21] See Supplemental Material at http://link.aps.org/supplemental/10.1103/PhysRevB.100.081105 for details of the synthesis, measurements and data analysis.

[22] K.-W. Chen, S. Das, D. Rhodes, S. Memaran, T. Besara, T. Siegrist, E. Manousakis, L. Balicas, and R. E. Baumbach, J. Phys.: Condens. Matter **28**, 14LT01 (2016).

[23] M. A. Hossain, J. D. F. Mottershead, D. Fournier, A. Bostwick, J. L. McChesney, E. Rotenberg, R. Liang, W. N. Hardy, G. A. Sawatzky, I. S. Elfimov, D. A. Bonn, and A. Damascelli, Nat. Phys. **4**, 527 (2008).

[24] D. Hsieh, L. Wray, D. Qian, Y. Xia, J. H. Dil, F. Meier, L. Patthey, J. Osterwalder, G. Bihlmayer, Y. S. Hor, R. J. Cava, and M. Z. Hasan, New J. Phys. **12**, 125001 (2010).

[25] J. Seo, P. Roushan, H. Beidenkopf, Y. S. Hor, R. J. Cava, and A. Yazdani, Nature (London) **466**, 343 (2010).